ARTICLES
https://doi.org/10.1038/s41560-019-0474-3
nature energy

All-temperature batteries enabled by fluorinated electrolytes with non-polar solvents

Xiulin Fan[1,2,4], Xiao Ji[1,4], Long Chen[1,4], Ji Chen[1], Tao Deng[1], Fudong Han[1], Jie Yue[1], Nan Piao[1], Ruixing Wang[3], Xiuquan Zhou[3], Xuezhang Xiao[2], Lixin Chen[2] and Chunsheng Wang[1,3*]

Carbonate electrolytes are commonly used in commercial non-aqueous Li-ion batteries. However, the high affinity between the solvents and the ions and high flammability of the carbonate electrolytes limits the battery operation temperature window to −20 to +50 °C and the voltage window to 0.0 to 4.3 V. Here, we tame the affinity between solvents and Li ions by dissolving fluorinated electrolytes into highly fluorinated non-polar solvents. In addition to their non-flammable characteristic, our electrolytes enable high electrochemical stability in a wide voltage window of 0.0 to 5.6 V, and high ionic conductivities in a wide temperature range from −125 to +70 °C. We show that between −95 and +70 °C, the electrolytes enable $LiNi_{0.8}Co_{0.15}Al_{0.05}O_2$ cathodes to achieve high Coulombic efficiencies of >99.9%, and the aggressive Li anodes and the high-voltage (5.4 V) $LiCoMnO_4$ to achieve Coulombic efficiencies of >99.4% and 99%, respectively. Even at −85 °C, the $LiNi_{0.8}Co_{0.15}Al_{0.05}O_2$|| Li battery can still deliver ~50% of its room-temperature capacity.

In recent decades, the number of electric vehicles has expanded exponentially due to the significant reduction in cost of Li-ion batteries (LIBs)[1–8]. More than 60% of manufactured LIBs have been deployed in applications in transportation electrificaiton[9–12]. Hybrid and electrical vehicles urgently call for high-energy LIBs that are safe and capable of operating over a wide operational temperature range[10,11]. Commercial Li-ion batteries with ethylene carbonate (EC)-based electrolytes can only operate in the temperature range −20 to +5 °C. In addition, EC-based electrolytes are highly flammable, which could cause fires or even explosions under harsh operational and abuse conditions. Extensive efforts have been devoted to expand the operational ranges of Li-ion batteries. The most successful methods are: adding small amount of additives in the electrolytes[13,14], externally heating and insulating the cells[15] and self-heating the cell[12,16]. However, these strategies also reduce the energy and power density of the LIBs. The use of liquefied CO_2 and fluoromethane gas as an electrolyte enables the Li-ion battery to retain ~60% of its room-temperature capacity at –60 °C (ref. [17]), representing a breakthrough in low-temperature Li batteries. However, such a low-temperature performance was achieved by sacrificing safety at room temperatures, since the batteries have to be protected by sophisticated protective structures due to high pressures of tens of bars. The −70 °C LIB was developed by using the low melting point of ethyl acetate-based electrolytes, but the poor stability of the ethyl acetate severely limits the voltage of the battery, to only ~2 V (refs. [18,19]). Broadly speaking, electrolytes that have good electrochemical performance at low temperatures normally deteriorate at high temperatures because the low melting temperature solvents normally also have high volatility, limiting their high-temperature behaviour. In addition, these low-temperature electrolytes are normally flammable. The narrow temperature windows of Li-ion battery electrolytes are attributed to the strong affinity between solvents and Li ions, which is required for high ionic conductivity.

Herein, we tamed the affinity between solvents and Li ions by dissolving the fluorinated carbonate electrolytes (LiFSI-FEC/FEMC or LiBETI-FEC/DEC; LiFSI, lithium bis(fluorosulfonyl)imide; LiBETI, lithium bis(pentafluoroethanesulfonyl)imide; DEC, diethyl carbonate; FEC, fluoroethylene carbonate; FEMC, methyl (2,2,2-trifluoroethyl) carbonate) into non-polar stable solvents (tetrafluoro-1-(2,2,2-trifluoroethoxy)ethane (D2) or methoxyperfluorobutane (M3)). The designed electrolyte exhibits a high ionic conductivity in a wide temperature range from −125 to +70 °C, a high electrochemical stability in a wide potential window of 0.0–5.6 V and a high non-flammable characteristic. Even at an ultralow temperature of −85 °C, the $LiNi_{0.8}Co_{0.15}Al_{0.05}O_2$|| Li battery can still deliver a capacity of 96 mAh g^{-1}, which is more that 50% of the reversible capacity at room temperature.

Taming the electrolytes

To achieve high ionic conductivity, the solvents should have a high dielectric constant (ε) to sufficiently dissociate the Li ions from the anions. However, this requirement leads to several detrimental physical or chemical characteristics, and significantly restricts the electrochemical performance of the batteries.[20] First, the high dielectric constant means strong affinity between the solvent molecules and the Li ions, and therefore the desolvation process on the electrode surface is suppressed, limiting the Li-ion intercalation kinetics[18]. Second, strong binding of the Li ions to the solvents reduces the Li-ion transference number to 0.2–0.4 (ref. [20]). Third, the high dielectric constant of the solvents inevitably enhances the dipole–dipole force among these highly polar molecules, increasing the freezing temperature of the solvents and thus reducing the low-temperature performance of the electrolytes. All of these intrinsic features pose long-standing challenges in non-aqueous electrolytes, limiting the voltage window, the liquid temperature range and safety.

All-fluorinated, non-flammable electrolytes have high ionic conductivity and a wide electrochemical stability window[21]. However, Li-ion batteries using these all-fluorinated electrolytes cannot work at temperatures below −30 °C due to the high affinities between the

[1]Department of Chemical and Biomolecular Engineering, University of Maryland, College Park, MD, USA. [2]State Key Laboratory of Silicon Materials and School of Materials Science and Engineering, Zhejiang University, Hangzhou, China. [3]Department of Chemistry and Biochemistry, University of Maryland, College Park, MD, USA. [4]These authors contributed equally: Xiulin Fan, Xiao Ji, Long Chen. *e-mail: cswang@umd.edu

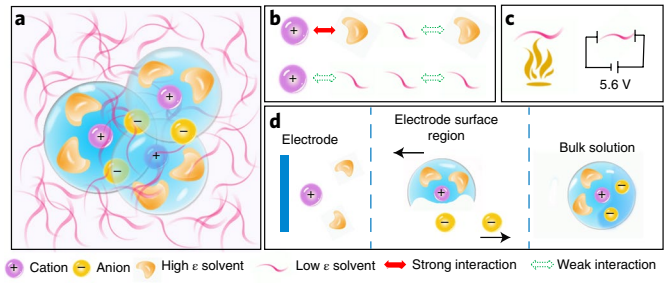

Fig. 1 | Electrolyte design strategy and the properties. a, Our electrolyte uses a non-polar solvent (D2 or M3, denoted by the purple curves) to tame the fluorinated carbonate electrolytes. The transparent blue spheres indicate the Li-ion solvation structure. The purple, positive-charged spheres indicate the Li ions. The brown, negative-charged spheres are anions. The solvated solvents with brown crescent shapes around the Li ions are the fluorinated carbonate solvents. **b**, The affinities between the solvents and ions. The Li ions and fluorinated carbonate solvents have a strong interaction (indicated by the solid red arrow), while the other three species have weak interactions between each other (dashed arrows). **c**, The non-flammable and high electrochemical stability requirements for the non-polar solvent in the superelectrolyte. The non-polar solvents are non-flammable and can withstand an extremely high voltage of 5.6 V. **d**, The expected electrochemical process at the electrode and electrolyte interface of the tamed electrolyte. In the bulk electrolyte, the Li ions will be solvated by fluorinated carbonate molecules and anions. At the surface region, the solvated Li ions will separate from the anions by means of the electric field. As the Li ions arrive at the surface of the electrode, the fluorinated carbonate molecules will finally be desolvated.

fluorinated solvents and the Li ions. To achieve a wide operational temperature range, we reduced the affinities between the solvents and the Li ions by dissolving the all-fluorinated electrolytes into highly fluorinated non-polar solvents, forming a superelectrolyte, as shown in Fig. 1a. The solvation structures of the all-fluorinated electrolyte are maintained in the electrolyte, since the interaction between the non-polar solvents and the Li ions was much weaker than that of Li ions and fluorinated carbonates, as illustrated in Fig. 1b. The non-polar solvents break the strong interaction between the highly polar molecules, widening the liquid-phase range and increasing the transference number. Therefore, the superelectrolytes maintain the electrochemical properties of the all-fluorinated electrolyte, but have significantly enhanced physical properties. Moreover, the highly fluorinated non-polar solvent itself also has a high electrochemical and chemical stability (Fig. 1c), further enhancing the safety and electrochemical potential window. The change of solvation structure in the superelectrolytes is also expected to improve the electrochemical process, including mass transfer and charge transfer (Fig. 1d).

To demonstrate the design principle for the electrolytes, 4.2 M LiFSI-FEC/FEMC and 2.33 M LiBETI-FEC/DEC were used as two model fluorinated electrolytes, and D2 and M3 were selected as two non-polar solvents to formulate the superelectrolytes. Specifically, 1.28 M LiFSI-FEC/FEMC–D2 electrolyte was prepared by dissolving of 4.2 M LiFSI-FEC/FEMC electrolyte into D2 solvent. The concentration of 1.28 M refers to all FEC, FEMC and D2 solvents. Similarly, 0.7 M LiBETI-FEC/DEC–M3 electrolyte was also prepared by dissolving 2.33 M LiBETI-FEC/DEC electrolyte into M3. Although no salts can be dissolved into pure D2 and M3, the 4.2 M LiFSI-FEC/FEMC and 2.33 M LiBETI-FEC/DEC electrolytes can be completely dissolved in D2 and M3, forming clear 1.28 M LiFSI-FEC/FEMC–D2 and 0.7 M LiBETI-FEC/DEC–M3 electrolytes, respectively. To distinguish from 1 M $LiPF_6$-EC/DMC (DMC, dimethyl carbonate) electrolyte, we use dash '–' to express the process of electrolyte dissolution into D2 or M3 non-polar solvent in 1.28 M LiFSI-FEC/FEMC–D2 and 0.7 M LiBETI-DEC/FEC–M3 electrolytes.

The fluorinated polar carbonate solvents in the superelectrolyte can sufficiently solvate the Li ions, providing high conductivity of the electrolyte. Meanwhile, the highly fluorinated non-polar solvents of D2 and M3 have a much lower molecular interaction, breaking the interactions between the fluorinated carbonate electrolyte and ensuring a wide liquid-phase temperature range, low viscosity and low Li^+ desolvation energy. When 4.2 M LiFSI-FEC/FEMC and 2.33 M LiBETI-FEC/DEC electrolytes were dissolved into a non-polar solvent (D2 or M3), the ion transport and other electrochemical properties mainly depended on the dissolved carbonate electrolyte (4.2 M LiFSI-FEC/FEMC or 2.33 M LiBETI-FEC/DEC), while the physical and chemical properties (such as freezing point, boiling point, flammability and Li-ion solvation/desolvation energy) essentially depended on the interactions between the dissolved electrolyte (4.2 M LiFSI-FEC/FEMC or 2.33 M LiBETI-FEC/DEC) and the non-polar solvents (D2 or M3). Disassociating the electrochemical properties from these physical and chemical properties can simultaneously achieve high-voltage stability and wide temperature windows, low viscosity and high ionic conductivity.

Physical and electrochemical properties of the electrolytes

Figure 2a shows the ionic conductivities of two superelectrolytes (1.28 M LiFSI-FEC/FEMC–D2 and 0.7 M LiBETI-FEC/DEC–M3), two representative liquid electrolytes (1 M $LiPF_6$-EC/DMC commercial electrolytes and 4.2 M LiFSI-FEC/FEMC high-concentration electrolytes) and two typical solid-state electrolytes $Li_7La_3Zr_2O_{12}$ (LLZO)[22] and $Li_{10}GeP_2S_{12}$ (LGPS)[23]. Since the ion transport of the three liquid electrolytes (1.28 M LiFSI-FEC/FEMC–D2, 0.7 M LiBETI-FEC/DEC–M3 and 4.2 M LiFSI-FEC/FEMC) is controlled by the mobility of the solvated molecules, the conductivity of these liquid electrolytes at different temperatures can be well described by the Vogel–Tammann–Fulcher empirical equation, as shown in Supplementary Fig. 1 (refs. [24,25]). The conductivities of crystalized 1.0 M $LiPF_6$-EC/DMC below −20 °C, LLZO and LGPS electrolytes follow the Arrhenius law. The conductivity of 1 M $LiPF_6$-EC/DMC electrolyte under −20 °C was fitted with the Arrhenius equation (Supplementary Fig. 1). Supplementary Table 1 lists the fitting parameters and calculated ionic conductivities of four liquid electrolytes. The crystallization of the 1 M $LiPF_6$-EC/DMC electrolyte and the solidification of 4.2 M LiFSI-FEC/FEMC due to a high glass transition temperature T_0 significantly reduced the conductivities of the 1 M $LiPF_6$-EC/DMC electrolyte and 4.2 M LiFSI-FEC/FEMC to less than 10^{-7} mS cm^{-1} at −80 °C (Supplementary Table 1).

The introduction of D2 into 4.2 M LiFSI-FEC/FEMC, and of M3 into 2.33 M LiBETI-FEC/DEC, slightly reduces the ionic conductivities of these electrolytes at room temperature. However, D2 and M3 can effectively suppress solidification of both liquid electrolytes, thus significantly enhancing the ionic conductivity of electrolytes at low temperatures. The conductivities of 1.28 M LiFSI-FEC/FEMC–D2 and 0.7 M LiBETI-FEC/DEC–M3 electrolytes at temperatures below −20 °C are 50 times higher than that of LLZO. In addition, the superelectrolytes have much lower interface resistance, higher fluidity and wider electrochemical windows than conventional carbonate electrolytes (Supplementary Fig. 3) and solid electrolytes (LLZO and LGPS)[26,27]. In conventional electrolytes, Li cations are coordinated with solvent and form a large solvation shell, reducing the mobility of the solvated Li cations, with a low transference number of 0.2–0.4. In superelectrolytes, the Li cations are solvated with less solvent molecules and meanwhile the anions are seriously dragged by the Li cations, which results in an unexpectedly high Li-ion transference number of ~0.7. At the extreme temperature of −80 °C, the conductivities of 1.28 M LiFSI-FEC/FEMC–D2 and 0.7 M LiBETI-FEC/DEC–M3 electrolytes are still $>1\times10^{-2}$ mS cm^{-1}, which is ten

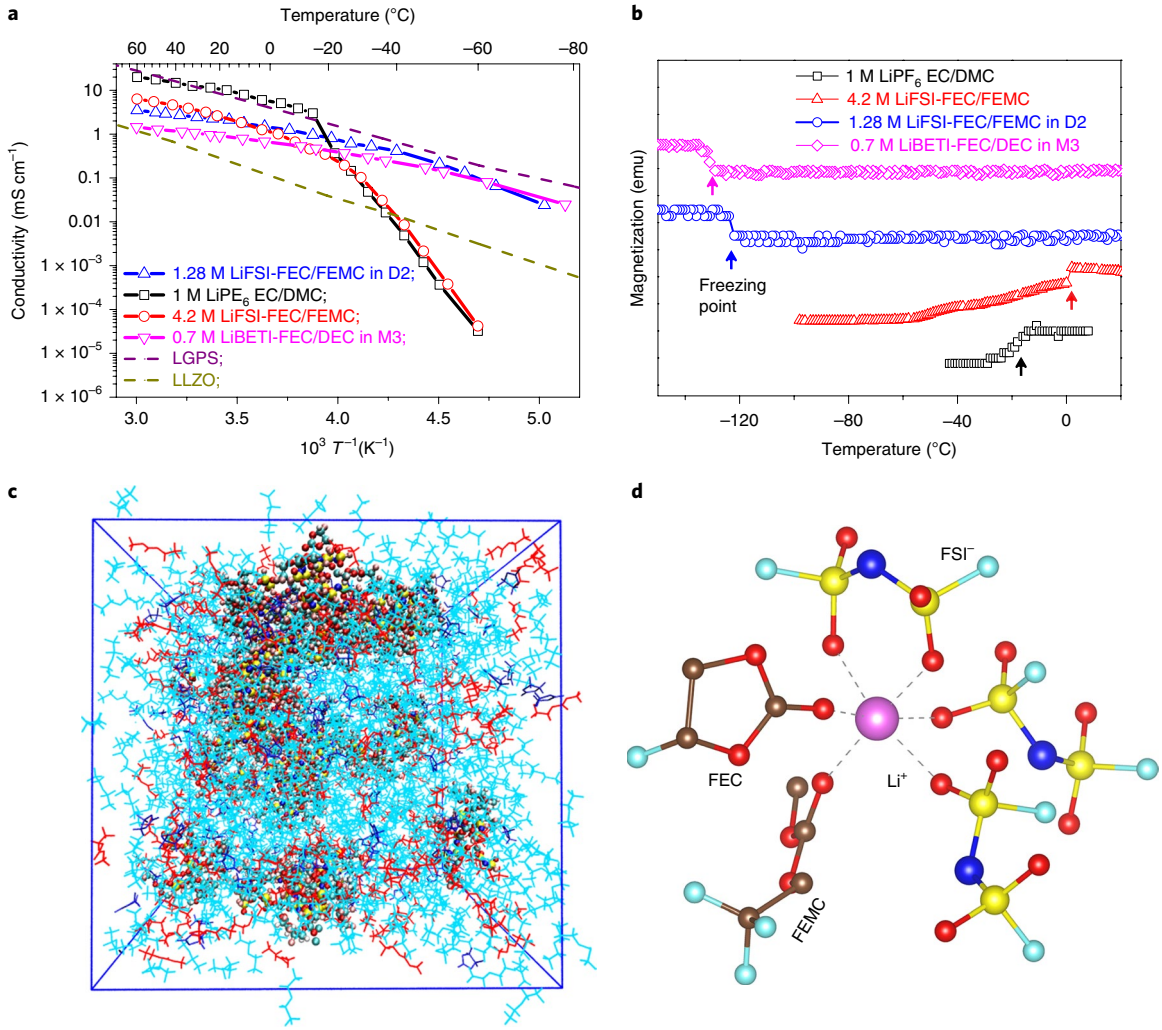

Fig. 2 | Physical properties and simulated structure of the superelectrolytes. a, Conductivity of liquid and solid electrolytes. **b**, Temperature dependence of the magnetic moment of the four different electrolytes measured in a superconducting quantum interference magnetometer device in an applied field of 1 mT. The freezing points of the electrolytes (as indicated by the arrows) can be determined by the transition point. The cooling rate is 1 °C min^{-1}. **c**, cMD simulated electrolyte structure for 1.28 M LiFSI-FEC/FEMC–D2. 125 LiFSI, 234 FEC, 280 FEMC and 793 D2 molecules were dissolved into a periodic box (65.1 × 65.1 × 65.1 Å^3). Li^+ ions and coordinated molecules (within 3 Å of Li^+ ions) are depicted by a ball-and-stick model, while the wireframes stand for the free solvents. Free D2, FEC and FEMC molecules are shown as cyan, blue and red wireframes, respectively, whereas hydrogens are excluded in the LiFSI-FEC/FEMC–D2 electrolyte. **d**, The representative Li^+ solvation structure extracted from the cMD simulations.

times higher than that of LiPON at room temperature[28,29], and sufficient to transport the ions between the anodes and the cathodes.

The high ionic conductivities of 1.28 M LiFSI-FEC/FEMC–D2 and 0.7 M LiBETI-FEC/DEC–M3 electrolytes at low temperatures are attributed to the extremely low melting point (Fig. 2b). The freezing points of these superelectrolytes were measured using a magnetic property measurement system (MPMS)[30] from discontinuity of $d\chi/dT$, where χ is the magnetic susceptibility and T the temperature (Supplementary Notes), as shown in Fig. 2c. The 1 M $LiPF_6$-EC/DMC electrolyte begins to freeze at about −15 °C, which is in good agreement with the differential scanning calorimetry (DSC) scan in Supplementary Fig. 4 and the freeze temperature reported in the literature[20]. The 4.2 M LiFSI-FEC/FEMC electrolyte shows a phase transition at an even higher temperature (~0 °C) due to the high freezing points of FEC (~22 °C) and FEMC. The high freezing points of the two electrolytes (1 M $LiPF_6$-EC/DMC and 4.2 M LiFSI-FEC/FEMC) coincide with their sudden drop in conductivity below −15 °C, as shown in Fig. 2a. Dissolving the 4.2 M LiFSI-FEC/FEMC electrolytes into D2 and the 2.33 M LiBETI-FEC/DEC into M3 dramatically lowers the freezing points of these two electrolytes to approximately −125 °C and approximately −132 °C, respectively. No deposits or phase separations emerge in these two electrolytes after being fully immersed in liquid at −95 °C for 3 h (Supplementary Figure 5).

The 1.28 M LiFSI-FEC/FEMC–D2 and 0.7 M LiBETI-FEC/DEC–M3 electrolytes also show low volatility at a high temperature, which is critical for the high-temperature performance of cells. As shown in Supplementary Fig. 6, the 1.28 M LiFSI-FEC/FEMC–D2 and 0.7 M LiBETI-FEC/DEC–M3 electrolytes show a volatility comparable to conventional the 1 M $LiPF_6$-EC/DMC electrolyte. The remaining mass of the electrolytes is higher than 50% as the temperature ramps up to 100 °C at 1.0 atm, and the residual mass will be significantly increased in a sealed cell due to the increased pressures. In addition, the much higher fluorine content in 1.28 M LiFSI-FEC/FEMC–D2 and 0.7 M LiBETI-FEC/DEC–M3 electrolytes than in the 1 M $LiPF_6$-EC/DMC electrolyte significantly increases the LiF content in the solid electrolyte interphase (SEI) and cathode electrolyte interphase (CEI) (as discussed below), which will further

increase the high-temperature stability of batteries due to the high thermal stability of the LiF-rich SEI/CEI and the lower solubility compared with organic-rich SEI.

The electrolytes 1.28 M LiFSI-FEC/FEMC–D2 and 0.7 M LiBETI-FEC/DEC–M3 electrolytes have wide temperature ranges of over 160 °C, which is comparable to the temperature range for the LGPS solid electrolyte[23]. However, the narrow thermodynamic stability window of LGPS (<0.5 V) limits its practical application in batteries[27]. Moreover, these liquid superelectrolytes have low interface resistance to the electrode and are capable of accommodating volume changes of the electrodes, which is not possible for LGPS solid electrolytes.

The structures of 1.28 M LiFSI-FEC/FEMC–D2 and 0.7 M LiBETI-FEC/DEC–M3 (Fig. 2c,d and Supplementary Figs. 7–9) superelectrolytes were simulated by classical molecular dynamics (cMD). The Li^+ and coordinated molecules in the first shell are depicted with a ball-and-stick model, while the free molecules are in a wireframe format. The coordinated structures are uniformly dispersed in each electrolyte, as we expected. The D2 and M3 are free solvent molecules, and do not coordinate with either the Li ions or the anions (Supplementary Table 2). Raman spectra confirmed that LiFSI-FEC/FEMC and LiBETI-FEC/DEC solvation clusters are uniformly dispersed into the D2 or M3 non-polar solvents (Supplementary Fig. 10). In other words, when 4.2 M LiFSI-FEC/FEMC and 2.33 M LiBETI-FEC/DEC electrolytes were dissolved into a non-polar solvent (D2 or M3), the electrochemical properties of the 1.28 M LiFSI-FEC/FEMC–D2 and 0.7 M LiBETI-FEC/DEC–M3 electrolytes were disassociated from the physical and chemical properties. In addition, the fluorinated polar carbonate solvents, highly fluorinated non-polar solvent and the LiFSI/LiBETI salts facilitate the formation of a LiF-rich SEI, and thereby enhance the high-temperature stability, maximizing the working electrochemical window.

The Li^+ solvation/desolvation energies of the conventional carbonate electrolyte and the disassociated electrolytes were calculated and are compared in Fig. 3a. The low ion-desolvation energy in the electrolytes is critical for the kinetics performance because the solvent molecules around Li^+ have to be completely stripped off before intercalation into the electrode materials. Especially at a low temperature, the sluggish desolvation process of Li^+ substantially limits its lithiation/delithiation reaction kinetics[18]. For the EC/DMC (3:1 molar) electrolyte, the solvation energy calculated from quantum chemistry is about −9.05 kcal mol^{-1}, which is in good agreement with the literature[31]. As the solvent blend changes to FEC/FEMC and FEC/DEC at a ratio of 1:3, the solvation energy dramatically reduces to −1.26 and −0.33 kcal mol^{-1}, which is only about 1/7 and 1/27 of the traditional EC/DMC (3:1 molar) electrolytes, respectively. By introducing FEC/FEMC or FEC/DEC polar solvents into non-polar solvent D2 or M3, complexes involved with D2 and M3 molecules further reduce the solvation energy to a positive value due to the weak interaction between Li^+ and D2 or M3 solvent molecules. The increase in positive solvation energy value with increase in the number of D2 or M3 molecules suggests that the interaction is energetically unfavourable for the Li^+ ion and D2 or M3 pair.

The structure and composition of the electrolytes not only affect the desolvation and diffusivity of the Li ions, but also change the SEI on the electrodes. The interphase layers on the electrodes also affect the reaction kinetics and cycle stability of the batteries. The SEI composition on the Li metal in 1.28 M LiFSI-FEC/FEMC–D2 is significantly different from that in the 1 M $LiPF_6$-EC/DMC electrolyte. The SEI in the 1 M $LiPF_6$-EC/DMC mainly consists of organic components, while the SEI film in the 1.28 M LiFSI-FEC/FEMC–D2 electrolyte is mainly composed of LiF-rich inorganic species (Supplementary Fig. 11). More specifically, the F:C atomic ratio in the SEI increases from 0.65 in the 1 M $LiPF_6$-EC/DMC, to 9.98 in the 1.28 M LiFSI-FEC/FEMC–D2 electrolyte. The LiF-rich SEI has high mechanical strength and high interfacial energy with Li metal, which can effectively suppress the Li dendrite, thus enhancing the Coulombic efficiency (CE) of Li plating/stripping[21,32]. The LiF-rich SEI also has a much higher thermal stability than organic-rich SEI at a high temperatures, which significantly enhances the high-temperature (60–70 °C) stability of the NCA ($LiNi_{0.8}Co_{0.15}Al_{0.05}O_2$)||Li cell, as discussed below. The extremely low electronic conductivity of LiF significantly reduces the thickness of the LiF-rich SEI, as evidenced by the appearance of Li metal within in a short sputtering time of SEI, as shown in Fig. 3b. The Li metal signal appears after only 5 min sputtering with Ar^+ on the SEI formed in the 1.28 M LiFSI-FEC/FEMC–D2 electrolyte (Fig. 3b). However, the Li metal signal does not show up until after 20 min sputtering of the SEI formed in the 1 M $LiPF_6$-EC/DMC electrolyte (Fig. 3c). Therefore, a thin and conformal LiF-rich SEI was formed on Li in the 1.28 M LiFSI-FEC/FEMC–D2 electrolyte, while a thick organic-rich SEI was formed on Li in the $LiPF_6$-EC/DMC electrolyte, as schematically demonstrated in Fig. 3d,e. Formation of the LiF-rich SEI in the 1.28 M LiFSI-FEC/FEMC–D2 electrolyte can be well explained by the cMD simulation of special solvation structures where most of the Li^+ cations (>99%) are partially coordinated with more than two FSI^- anions (Supplementary Table 2), enabling more FSI^- to participate in the SEI-forming reaction (Supplementary Fig. 12). Similarly to the SEI layer, the CEI layer is also mainly composed of inorganic species (Supplementary Fig. 13). These LiF-rich interphases bring several other benefits:[32,33] the Arrhenius behaviour of ionic conductivity for LiF-rich interphases enhances the ionic conductivity at low temperatures and the high thermal stability of the LiF-rich interphases improves the high-temperature electrochemical performance of both the anode and the cathode.

Low-temperature behaviour

The formation of the LiF-rich SEI on Li anodes in the 1.28 M LiFSI-FEC/FEMC–D2 electrolytes significantly increases the Li plating/stripping CE to 99.4% (Supplementary Fig. 14), which is one of the highest CEs reported so far for Li plating/striping[34]. Figure 4a–e shows the electrochemical performance of the NCA||Li coin cells in different electrolytes at an area capacity of ~1.2 mAh cm^{-2}. The specific capacity and current density are calculated from the mass of the active cathode materials. At room temperature (25 °C), the discharge capacities of NCA||Li cells in both 1 M $LiPF_6$-EC/DMC and 1.28 M LiFSI-FEC/FEMC–D2 are about 172 mAh g^{-1}. However, when the temperature is reduced to −42 °C, the NCA||Li cells in 1.28 M LiFSI-FEC/FEMC–D2 electrolyte can still provide a high capacity of 160 mAh g^{-1}, while the NCA||Li cells in the 1 M $LiPF_6$-EC/DMC electrolyte can only provide a capacity of 13.3 mAh g^{-1}. The rapid decay in capacity of NCA||Li cells at −42 °C in the 1 M $LiPF_6$-EC/DMC electrolyte (Fig. 4c) is because the electrolyte is completely solidified at −30 °C. Even when the temperature is decreased to −85 °C, the NCA||Li cell using 1.28 M LiFSI-FEC/FEMC–D2 can still deliver a capacity of 96 mAh g^{-1}, while the NCA||Li cell in 1 M $LiPF_6$-EC/DMC cannot provide any capacity below −67 °C. This shows extreme battery performance at a temperature below the condensation point of CO_2 (−78 °C). Figure 4d demonstrates that a small NCA||Li pouch cell can power an electric fan at −95 °C.

The NCA||Li cells using 1.28 M LiFSI-FEC/FEMC–D2 electrolyte also show much longer cycling stability than those in 1 M $LiPF_6$-EC/DMC at −20 °C at a 1/3 C (1 C = 170 mAh g^{-1}) rate. As demonstrated in Fig. 4e, NCA||Li cells using the 1.28 M LiFSI-FEC/FEMC–D2 electrolyte can maintain a high capacity of 150 mAh g^{-1} for 450 cycles, while NCA||Li cells using the 1 M $LiPF_6$ EC/DMC electrolyte can only provide 35 mAh g^{-1} for 100 cycles and then the capacity drops rapidly. The superelectrolytes also enable more aggressive Li-ion cathodes and Na-ion cathodes to achieve high performance at a very low temperature. Supplementary Fig. 15 shows that a $LiNi_{0.6}Mn_{0.2}Co_{0.2}O_2$ (NMC622)||Li cell using 0.7 M

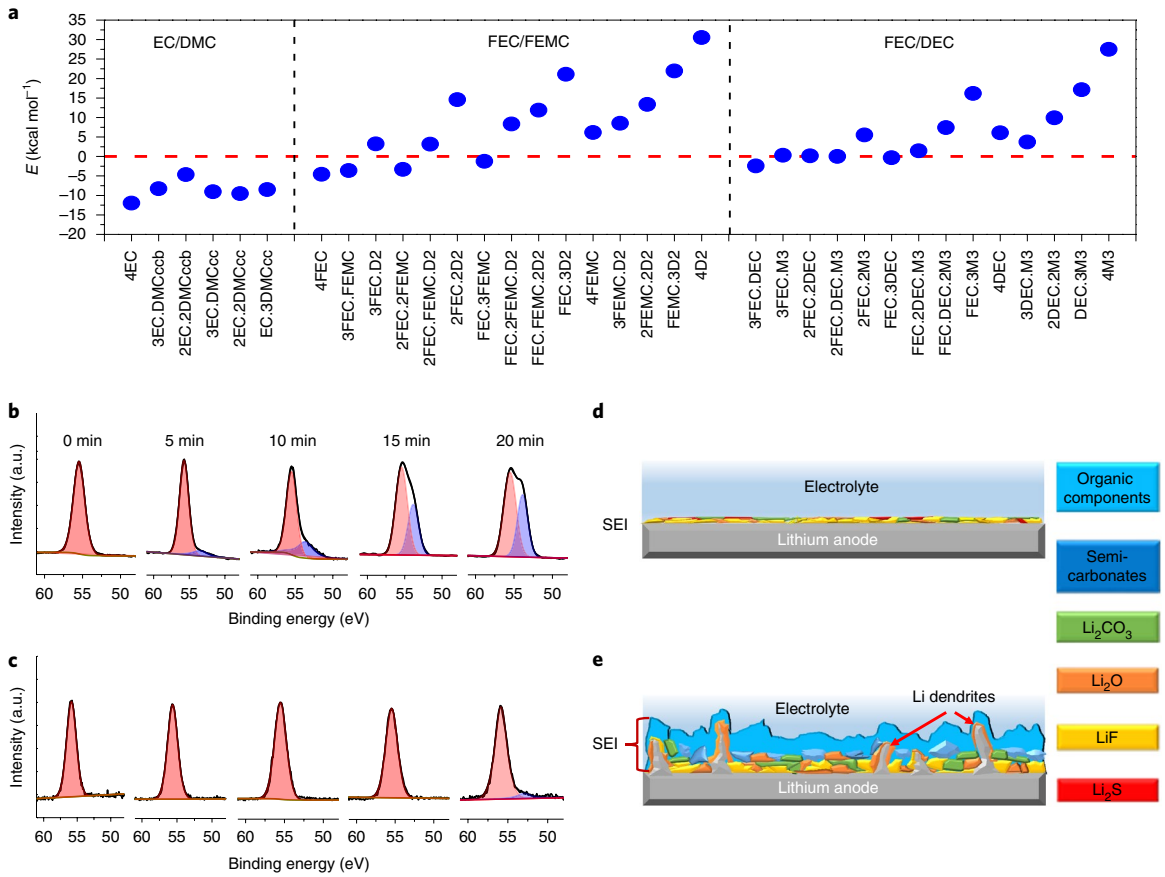

Fig. 3 | Li-ion solvation/desolvation energy in different electrolytes and the interphase analysis. a, The calculated Li^+ solvation/desolvation energy with different structures of the $LiPF_6$-EC/DMC and superelectrolytes; DMCcc and DMCccb stand for the two DMC *cis–cis* conformers[58]. **b**,**c**, XPS Li 1s spectra of cycled lithium metal anode before sputtering and after different sputtering times using 1.28 M LiFSI-FEC/FEMC–D2 electrolyte (**b**) and 1 M $LiPF_6$-EC/DMC electrolyte (**c**). **d**,**e**, Schematic illustration of SEI layers formed in different electrolytes: 1.28 M LiFSI-FEC/FEMC–D2 electrolyte (**d**) and 1 M $LiPF_6$-EC/DMC electrolyte (**e**).

LiBETI-FEC/DEC–M3 electrolytes can power 51 light-emitting diodes at −80 °C. When the LiFSI salt was replaced by the NaFSI salt, the $Na_3V_2(PO_4)_2O_2F$||Na cells using the 1.28 M NaFSI-FEC/FEMC–D2 electrolytes also showed significantly better low-temperature performance than cells using 1.0 M $NaPF_6$-EC/DMC (Supplementary Fig. 16). At −58 °C, $Na_3V_2(PO_4)_2O_2F$||Na cells can still provide 70 mAh g^{-1}, which is more than 50% of the capacity at 25 °C. The extremely low alkaline ion solvation/desolvation energy (Fig. 3a), extended liquid temperature range (Fig. 2b) and the compact SEI/CEI (Fig. 3b) contribute to these highly reversible Li batteries at ultralow temperatures.

High-temperature behaviour

NCA||Li cells using 1.28 M LiFSI-FEC/FEMC–D2 and 0.7 M LiBETI-FEC/DEC–M3 electrolytes also show a superior performance at high temperatures. As shown in Fig. 4c and Supplementary Fig. 17, the capacity of the NCA||Li cell at 70 °C using 1.28 M LiFSI-FEC/FEMC–D2 is similar to that using 1.0 M $LiPF_6$-EC/DMC. During charge/discharge cycles, the NCA||Li cell using the 1.28 M LiFSI-FEC/FEMC–D2 electrolyte maintains a high capacity of 170 mAh g^{-1}, while the capacity of the NCA||Li cell using 1.0 M $LiPF_6$-EC/DMC electrolyte rapidly decays to 50% capacity in less than five cycles, due to the instability of the SEI/CEI at high temperatures. At 60 °C, NCA||Li cells in 0.7 M LiBETI-FEC/DEC–M3 electrolytes also show a significantly batter cycling stability than cells using 1 M $LiPF_6$-EC/DMC electrolytes (Supplementary Fig. 17).

High-voltage cell behaviour

In addition, the superelectrolyte also possesses a wide electrochemical voltage window in a broadened operational temperature range. A high-voltage cathode (5.4 V) of $LiCoMnO_4$ is utilized to evaluate the high-voltage stability of the electrolytes over a wide temperature range. Figure 4f,g shows the cyclic voltammetry curves of 5.4 V $LiCoMnO_4$||Li cells in 1.0 M $LiPF_6$-EC/DMC and 1.28 M LiFSI-FEC/FEMC–D2 electrolytes at different temperatures. $LiCoMnO_4$||Li cells using 1 M $LiPF_6$-EC/DMC experience significantly increased oxidation peaks, with extremely low CE at high voltages above 4.8 V as the temperature increases from 25 °C to 60 °C, while no redox peak is observed when the temperature drops to −30 °C (Fig. 4f). In contrast, a significantly highly reversible capacity is observed for $LiCoMnO_4$ using the 1.28 M LiFSI-FEC/FEMC–D2 electrolyte even at −60 °C (Fig. 4g), although the overpotential of the spinel cathode is increased and the two-step lithiation/delithiation is merged into one step due to the reduced Li-ion diffusion kinetics[35]. The lithiation/delithiation behaviour of $LiCoMnO_4$||Li cells at +60 °C is similar to that at 25 °C, demonstrating the superior stability of the 1.28 M LiFSI-FEC/FEMC–D2 electrolyte at high temperatures and high voltage. Besides, the superelectrolyte also enables graphite and 5 V $LiNi_{0.5}Mn_{1.5}O_4$ to achieve higher CEs and cycling stability than in 1 M $LiPF_6$-EC/DMC electrolyte (Supplementary Figs. 18 and 19).

Supplementary Fig. 21 shows the operation temperature limits of different rechargeable batteries, with the highest and lowest temperatures recorded on Earth for reference. No batteries can operate in such a harsh temperature range. Alkaline Ni-MH batteries still

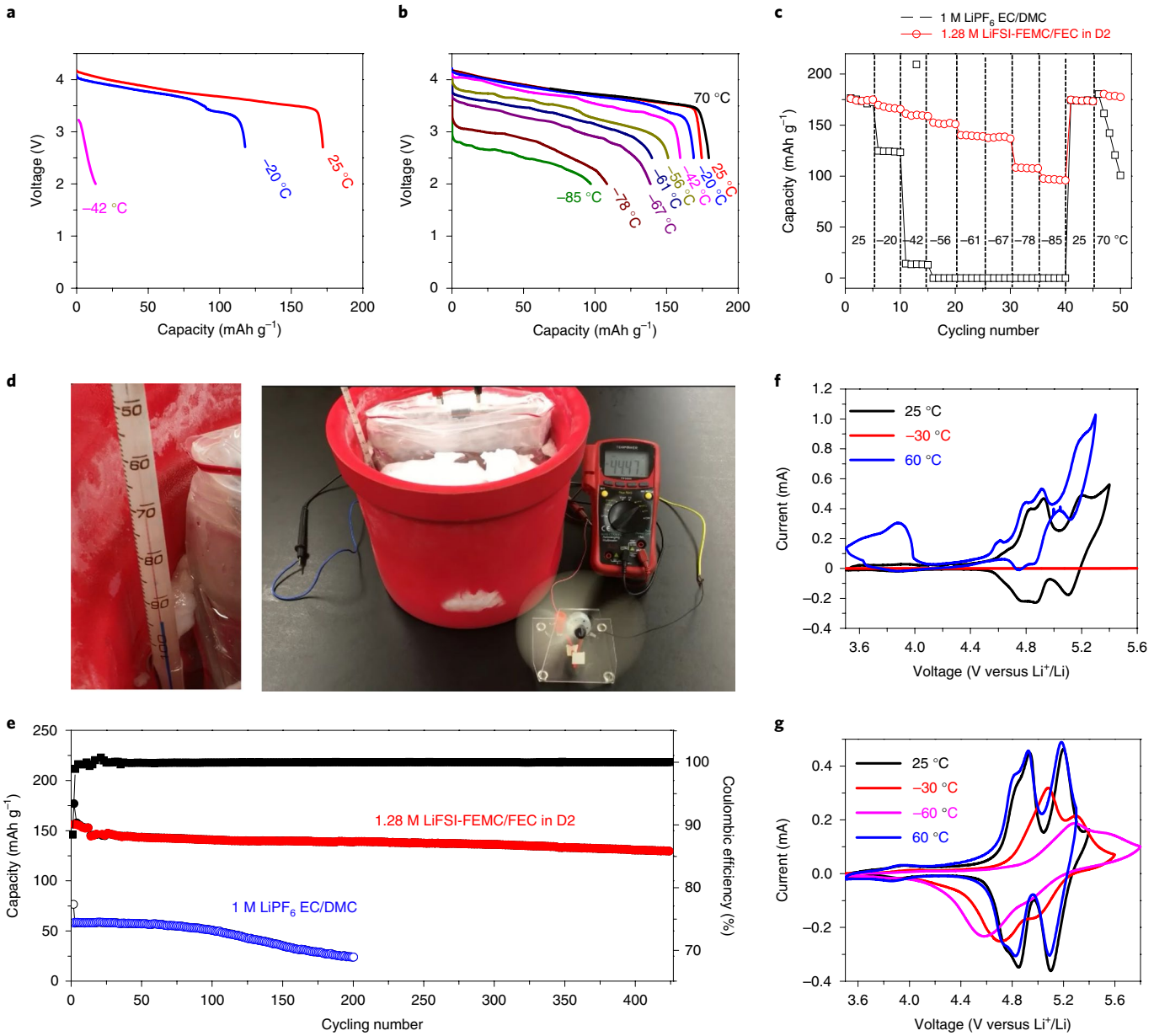

Fig. 4 | Electrochemical performance of NCA || Li cells using different electrolytes at different temperatures. a, Discharge profiles of NCA || Li cells using conventional 1 M $LiPF_6$-EC/DMC electrolyte at different temperatures. **b**, Discharge profiles of NCA || Li cells using 1.28 M LiFSI-FEC/FEMC-D2 electrolyte at different temperatures. **c**, Discharge capacities of NCA || Li cells using 1.28 M LiFSI-FEC/FEMC-D2 and 1.0 M $LiPF_6$-EC/DMC electrolytes at different temperatures. **d**, Optical images of an electric fan powered by the NCA || Li pouch cell using 1.28 M LiFSI-FEC/FEMC-D2 electrolyte at −95 °C. The video is in Supplementary Video 1, and the size of the pouch cell is shown in Supplementary Fig. 20. **e**, Cycling performance of NCA || Li using 1 M $LiPF_6$-EC/DMC and 1.28 M LiFSI-FEC/FEMC-D2 electrolytes at −20 °C with a charge/discharge current density of 1/3 C. **f**,**g**, Cyclic voltammetry curves of $LiCoMnO_4$ || Li at different temperatures using different electrolytes at a scanning rate of 0.05 mV s^{-1} using 1 M $LiPF_6$-EC/DMC electrolyte (**f**) and 1.28 M LiFSI-FEC/FEMC-D2 electrolyte (**g**).

cannot operate below −30 °C due to being intrinsically prone to freezing of the aqueous electrolyte[36]. The operation temperature range of well-matured lead-acid batteries is only from −40 °C to +65 °C. Commercial LIBs can sustain a much narrower temperature range, between −20 °C and +55 °C with severe capacity decay at temperatures below 0 °C (ref. [37]). Considering the highest (56.7 °C, Death Valley, California, USA, 1913) and lowest temperatures (−89.2 °C, Vostok Station, Antarctica, 1983) ever recorded on Earth, superelectrolyte Li batteries with an operational temperature range from −95 °C to +70 °C are highly reversible batteries that could operate at any place in our planet.

Another important requirement for electrolytes is non-flammability[21,38–41]. The superelectrolytes with physical and chemical properties disassociated from electrochemical properties can simultaneously achieve high electrochemical performance in a wide temperature and voltage window, and are non-flammable as well. Supplementary Fig. 22 compares the electrochemical properties of superelectrolytes with the most promising electrolytes, including aqueous electrolytes, sulfide-based solid-state LGPS and LPS electrolytes (Supplementary Figs. 23 and 24), traditional carbonate electrolytes and ether-based electrolytes. The superelectrolytes are non-flammable and have the widest electrochemical window

from 0.0 V Li metal anode to the ultrahigh-voltage cathode of 5.4 V $LiCoMnO_4$ with the highest CEs, outperforming all other electrolytes, including solid-state electrolytes and water-in-salts aqueous electrolytes. The flammability tests of these electrolytes are shown in Supplementary Videos 2–6. The sulfide-based LGPS/LPS solid-state electrolytes are still flammable and will generate highly toxic gases such as SO_2 and H_2S during burning or exposure to moisture. Therefore, sulfide solid-state electrolyte batteries still face safety concerns.

Conclusions

By dissolving fluorinated carbonate electrolytes into highly fluorinated non-polar solvents, we developed superelectrolytes where the electrochemical properties of the electrolytes are disassociated from their physical and chemical properties. At room temperature, the superelectrolytes enable the most promising electrodes to achieve a high cycling CE (99.4% for Li metal, >99.9% for graphite, >99.9% for $LiNi_{0.8}Mn_{0.1}Co_{0.1}O_2$, 99.9% for 5.0 V $LiNi_{0.5}Mn_{1.5}O_4$ and 99% for 5.4 V $LiCoMnO_4$). The NCA||Li battery using superelectrolytes at −85 °C can deliver 56% of its room-temperature capacity and maintain high cycling stability at 60 °C. The highly fluorinated non-polar solvents associated with the fluorinated electrolyte make the electrolyte non-flammable, greatly improving the safety of the batteries. The present design therefore represents an encouraging path towards creating safe Li batteries with a sufficiently wide operational temperature range.

Methods

Materials. Li chips with a thickness of 250 μm were purchased from MTI. Cathode NCA ($LiNi_{0.8}Co_{0.15}Al_{0.05}O_2$) and LNMO ($LiNi_{0.5}Mn_{1.5}O_4$) powders were purchased from MTI. Graphite (TIMREX KS15) was obtained from Timcal. Ethylene carbonate, dimethyl carbonate (DMC), diethyl carbonate (DEC), fluoroethylene carbonate (FEC) and methoxyperfluorobutane (C_4F_9-O-CH_3, 1,1,1,2,2,3,3,4,4-nonafluoro-4-methoxybutane, M3) were purchased from Sigma-Aldrich. Methyl (2,2,2-trifluoroethyl) carbonate (FEMC), lithium bis(pentafluoroethanesulfonyl)imide (LiBETI, >98%) and 1,1,2,2-tetrafluoro-1-(2,2,2-trifluoroethoxy)ethane (D2) were obtained from Tokyo Chemical Industry. $LiPF_6$ (99.999%) was purchased from BASF USA. $NaPF_6$ (>99%) was purchased from Sigma-Aldrich. Lithium bis(fluorosulfonyl)imide (LiFSI, >99.99%) was purchased from Chunbo. Sodium bis(fluorosulfonyl)imide (NaFSI, 99.7%) was purchased from Solvionic. For a typical LiFSI-FEMC/FEC in D2 electrolyte, 1 ml FEC and 2 ml FEMC were mixed together, then 2.4 g LiFSI was dissolved into the mixed solvents. After the LiFSI had completely dissolved, the LiFSI-FEMC/FEC electrolyte was added into 7 ml of D2 solvent under stirring, forming the LiFSI-FEMC/FEC in D2 electrolyte. For the LiBETI-DEC/FEC in M3 electrolyte, 2.7 g LiBETI was dissolved into FEC:DEC:M3 (0.5 ml:2.5 ml:7 ml) solvent. The ionic conductivities of the electrolytes at different temperatures were calculated by electrochemical impedance spectroscopy measurements with two platinum plate electrodes (1 cm^2) symmetrically placed in the electrolyte solutions.

The $LiCoMnO_4$ was synthesized by a two-step method based on a previous report[42]. The solid-state electrolytes $Li_{10}GeP_2S_{12}$ (LGPS) and Li_3PS_4 (LPS) were synthesized following previously reported procedures[23,43].

Characterizations. X-ray photoelectron spectroscopy (XPS) was conducted on a high sensitivity Kratos Axis 165 X-ray photoelectron spectrometer with Mg Kα radiation. All binding-energy values were referenced to the C 1*s* peak of carbon at 284.6 eV. Before the XPS characterizations, the cycled electrodes were washed with the corresponding solvents to remove residual salts. The differential scanning calorimetry measurements were carried out in a DSC 404 F1 Pegasus (NETZSCH) differential scanning calorimeter using a scanning rate of 1 °C min^{-1}. Powder X-ray diffraction data were collected on a Bruker D8 X-ray diffractometer (Cu Kα radiation, wavelength $\lambda = 1.5418$ Å). Freezing points of electrolytes were determined by respective first-order transitions of temperature-dependent magnetic susceptibility using a magnetic property measurement system (Quantum Design MPMS). The scanning rate was 1 °C min^{-1}.

Electrochemical measurements. Electrolytes were prepared by adding the salt into various anhydrous solvents. All the solvents were dried by molecular sieve (4 Å, Sigma-Aldrich) to make sure the water content was lower than 10 ppm, which was tested using a Karl Fischer titrator (Metrohm 899 Coulometer). The charge–discharge performances of the Li batteries were examined using 2,032-type coin cells. The same coin-type cells were used to investigate the cycling stability of Li plating/stripping in different electrolytes. For the low-temperature discharge test, the battery was charged at room temperature with a current density of 1/3 C, and discharged at different temperatures with a current of 1/15 C. The CE of the Li plating and stripping was calculated from the ratio of the Li removed from the Cu substrate to that deposited in the same cycle. A three-electrode 'T-cell' was utilized to test the stability window of the different electrolytes with polished stainless steel as the working electrode and Li foils as the reference and counter electrodes using a Gamry 1000E electrochemical workstation (Gamry Instruments). The Li^+ transference number was calculated by testing the alternating-current (AC) impedance and direct-current (DC) impedance of the Li||Li symmetric battery and by using the formula $t_{Li+} = R_{cell}/R_{DC}$ (ref. [44]), where t is the transference number and R the resistance. R_{cell} was obtained by electrochemical impedance spectroscopy with a frequency of 10 MHz to 0.1 Hz and an AC signal amplitude of 5 mV. R_{DC} was obtained by performing a 10 mV DC polarization for 10,800 s to obtain a steady current ($R_{DC} = V_{DC}/I_{DC}$, V is voltage and I is current). Both AC and DC impedence were performed using a CHI660E electrochemical workstation. The area capacity of the $LiNi_{0.8}Co_{0.15}Al_{0.05}O_2$ (NCA) in the pouch cell was about 2 mAh cm^{-2}, and the total pouch cell capacity was 400 mAh. All the cells were assembled in a glove box with a water/oxygen content lower than 1 ppm. The galvanostatic charge–discharge test was conducted on a battery test station (BT2000, Arbin Instruments).

Flammability test. For the liquid electrolytes, the flammability was tested on the electrolyte-soaked glass fibre filter. For the solid-state sulfide electrolytes of LPS and LGPS, small pellets with a diameter of 1 cm were prepared by cold pressing of about 200 mg powder with a pressure of ~800 MPa. The flammability of the solid-state sulfide electrolytes was directly tested based on these pellets.

Computational methods. To investigate the electrolytes of LiFSI-FEC/FEMC in D2 and LiBETI-FEC/DEC in M3 at an atomic scale, three types of calculations were performed. (1) cMD simulation to study the electrolyte structures using large-scale atomic/molecular massively parallel simulator (LAMMPS, http://lammps.sandia.gov.)[45]. (2) Quantum chemistry calculations to predict solvation energy of possible solvation configurations in FEMC/FEC–D2 solvent using the Gaussian 09 package[46]. (3) Ab initio molecular dynamic (AIMD) simulation to show the structure and Li^+ motion of the electrolyte utilizing the Vienna ab initio simulation package (VASP)[47–49]. Visualization of the structures was made using VESTA and VMD software[50,51].

cMD simulations. cMD simulations were conducted on the electrolytes using the LAMMPS simulation package. General amber force fields parameters[52] and AM1-BCC charges[52,53] were used and generated by the ANTECHAMBER program in AmberTools for the solvent molecules[54]. The force fields for Li, FSI and BETI were taken from previous publications[55–57]. For the LiFSI-FEMC/FEC in D2 electrolyte, 125 LiFSI, 234 FEC, 280 FEMC and 793 D2 molecules were dissolved into a periodic box, while for LiBETI-DEC/FEC in M3 electrolyte, 78 LiBETI, 70 FEC, 205 DEC and 364 M3 molecules were calculated. The systems were set up initially with simulation boxes 80 and 58 Å in length, with the salt and solvent molecules distributed in the simulation boxes using Moltemplate (http://www.moltemplate.org/). First, NPT runs were performed at 330 K for 5 ns and then 298 K for 5 ns to ensure that the equilibrium salt dissociation had been reached. Then, the NVT runs were 10 ns long at 298 K and the last 5 ns were used to obtain the structure of the electrolyte. The anions were not considered in the desolvation energy calculation because the anions in the interface will depart from the cations once the electric field is applied in the electrode and the electrolyte interface, as illustrated in Fig. 1, which is confirmed by the high transference number. The computation schemes have been widely used in previous related works[58].

Quantum chemistry calculations. All quality control calculations were performed using the Gaussian 09 software package. The Perdew–Burke–Ernzerhof functional was used as it was shown to accurately describe electron affinity and ionization potential. The double-zeta basis set 6–31 + G(d,p) was used for structure optimization as well as the energy calculation. The SMD implicit solvation model was used to describe the solvation effect. Acetone ($\varepsilon = 20.49$) was used as the solvent for calculation of Li complexes.

AIMD simulation. The electrolyte cell with a single LiFSI molecule was dissolved in a periodic box of 3 FEC, 3 FEMC and 9 D2 molecules. The system corresponds to 220 total atoms, with a density of 1.55 g cm^{-3}. We performed the AIMD calculation using the VASP package. The ion–electron interaction was described with the projector augmented wave method, and the exchange-correlation energy was described by the functional of the Perdew–Burke–Ernzerhof form of the generalized gradient approximation[59–61]. The plane wave energy cut-off of 400 eV was chosen and a minimal Γ-centred 1 × 1 × 1 *k*-point grid was used. All molecular dynamics simulations were performed in the NVT ensemble using a Nosé—Hoover thermostat. Each system was heated to 300 K and equilibrated for 20 ps and then simulated for 30 ps to gather statistics. AIMD simulations were performed on the electrolyte of LiFSI-FEMC/FEC in D2 to understand the mechanisms for superior performance. The electrolyte structure was simulated by assuming that Li^+ and FSI^- ions are initially associated or initially dissociated (Supplementary Fig. 12). This showed that Li^+ tends to remain associated or to re-associate with FSI^- and is coordinated with the FEMC and FEC. Even when Li^+ and FSI^- are initially dissociated, the Li^+ and FSI^- with a distance of ~3.5 Å follow similar trajectories to

the associated Li^+ and FSI^- after 10 ps, changing to a correlated ion motion. These results are in good agreement with the cMD simulations and further confirmed the Li^+ coordinated with FSI^- anions, FEC and FEMC molecules, while without coordination with D2 molecules.

Data availability

The data that support the plots within this paper and other findings of this study are available from the corresponding author upon reasonable request.

Received: 28 April 2019; Accepted: 2 September 2019;
Published online: 7 October 2019

References

1. Whittingham, M. S. Ultimate limits to intercalation reactions for lithium batteries. *Chem. Rev.* **114**, 11414–11443 (1976).
2. Cheng, X. B., Zhao, C. Z., Yao, Y. X., Liu, H. & Zhang, Q. Recent advances in energy chemistry between solid-state electrolyte and safe lithium metal anodes. *Chem* **5**, 74–96 (2019).
3. Assat, G. & Tarascon, J. M. Fundamental understanding and practical challenges of anionic redox activity in Li-ion batteries. *Nat. Energy* **3**, 373–386 (2018).
4. Armand, M. & Tarascon, J. M. Building better batteries. *Nature* **451**, 652–657 (2008).
5. Lin, D., Liu, Y. & Cui, Y. Reviving the lithium metal anode for high-energy batteries. *Nat. Nanotechnol.* **12**, 194–206 (2017).
6. Choi, J. W. & Aurbach, D. Promise and reality of post-lithium-ion batteries with high energy densities. *Nat. Rev. Mater.* **1**, 16013 (2016).
7. Sun, Y.-K. et al. Nanostructured high-energy cathode materials for advanced lithium batteries. *Nat. Mater.* **11**, 942–947 (2012).
8. Zhu, C., Usiskin, R. E., Yu, Y. & Maier, J. The nanoscale circuitry of battery electrodes. *Science* **358**, eaao2808 (2017).
9. Lee, J. et al. Reversible Mn^{2+}/Mn^{4+} double redox in lithium-excess cathode materials. *Nature* **556**, 185–190 (2018).
10. Dunn, B., Kamath, H. & Tarascon, J.-M. Electrical energy storage for the grid: a battery of choices. *Science* **334**, 928–935 (2011).
11. Noorden, R. V. The rechargeable revolution: a better battery. *Nature* **507**, 26–28 (2014).
12. Yang, X.-G., Zhang, G., Ge, S. & Wang, C.-Y. Fast charging of lithium-ion batteries at all temperatures. *Proc. Natl Acad. Sci. USA* **115**, 7266–7271 (2018).
13. Zhang, S. S., Xu, K. & Jow, T. R. A new approach toward improved low temperature performance of Li-ion battery. *Electrochem. Commun.* **4**, 928–932 (2002).
14. Smart, M. C., Whitacre, J. F., Ratnakumar, B. V. & Amine, K. Electrochemical performance and kinetics of $Li_{1+x}(Co_{1/3}Ni_{1/3}Mn_{1/3})_{1-x}O_2$ cathodes and graphite anodes in low-temperature electrolytes. *J. Power Sources* **168**, 501–508 (2007).
15. Stuart, T. A. & Hande, A. HEV battery heating using AC currents. *J. Power Sources* **129**, 368–378 (2004).
16. Wang, C.-Y. et al. Lithium-ion battery structure that self-heats at low temperatures. *Nature* **529**, 515–518 (2016).
17. Rustomji, C. S. et al. Liquefied gas electrolytes for electrochemical energy storage devices. *Science* **356**, aal4263 (2017).
18. Dong, X., Guo, Z., Guo, Z., Wang, Y. & Xia, Y. Organic batteries operated at −70 °C. *Joule* **2**, 902–913 (2018).
19. Dong, X. et al. High energy rechargeable metallic lithium battery at −70 °C enabled by a co-solvent electrolyte. *Angew. Chem.* **131**, 5679–5683 (2019).
20. Xu, K. Nonaqueous liquid electrolytes for lithium-based rechargeable batteries. *Chem. Rev.* **104**, 4303–4418 (2004).
21. Fan, X. et al. Non-flammable electrolyte enables Li-metal batteries with aggressive cathode chemistries. *Nat. Nanotechnol.* **13**, 715–722 (2018).
22. Ramakumar, S., Satyanarayana, L., Manorama, S. V. & Murugan, R. Structure and Li^+ dynamics of Sb-doped $Li_7La_3Zr_2O_{12}$ fast lithium ion conductors. *Phys. Chem. Chem. Phys.* **15**, 11327–11338 (2013).
23. Kamaya, N. et al. A lithium superionic conductor. *Nat. Mater.* **10**, 682–686 (2011).
24. Croce, F., Focarete, M. L., Hassoun, J., Meschini, I. & Scrosati, B. A safe, high-rate and high-energy polymer lithium-ion battery based on gelled membranes prepared by electrospinning. *Energy Environ. Sci.* **4**, 921–927 (2011).
25. Gu, G. Y. et al. 2-Methoxyethyl (methyl) carbonate-based electrolytes for Li-ion batteries. *Electrochim. Acta* **45**, 3127–3139 (2000).
26. Miara, L. J., Richards, W. D., Wang, Y. E. & Ceder, G. First-principles studies on cation dopants and electrolyte|cathode interphases for lithium garnets. *Chem. Mater.* **27**, 4040–4047 (2015).
27. Richards, W. D., Miara, L. J., Wang, Y., Kim, J. C. & Ceder, G. Interface stability in solid-state batteries. *Chem. Mater.* **28**, 266–273 (2016).
28. Hamon, Y. et al. Influence of sputtering conditions on ionic conductivity of LiPON thin films. *Solid State Ion.* **177**, 257–261 (2006).
29. Dudney, N. J. Addition of a thin-film inorganic solid electrolyte (Lipon) as a protective film in lithium batteries with a liquid electrolyte. *J. Power Sources* **89**, 176–179 (2000).
30. Cini, R. & Torrini, M. Temperature dependence of the magnetic susceptibility of water. *J. Chem. Phys.* **49**, 2826–2830 (1968).
31. Skarmoutsos, I., Ponnuchamy, V., Vetere, V. & Mossa, S. Li^+ solvation in pure, binary, and ternary mixtures of organic carbonate electrolytes. *J. Phys. Chem. C* **119**, 4502–4515 (2015).
32. Lu, Y., Tu, Z. & Archer, L. A. Stable lithium electrodeposition in liquid and nanoporous solid electrolytes. *Nat. Mater.* **13**, 961–969 (2014).
33. Choudhury, S. & Archer, L. A. Lithium fluoride additives for stable cycling of lithium batteries at high current densities. *Adv. Electron. Mater.* **2**, 1500246 (2016).
34. Fan, X. et al. Highly fluorinated interphases enable high-voltage Li-metal batteries. *Chem* **4**, 174–185 (2018).
35. Bi, K., Zhao, S. X., Huang, C. & Nan, C. W. Improving low-temperature performance of spinel $LiNi_{0.5}Mn_{1.5}O_4$ electrode and $LiNi_{0.5}Mn_{1.5}O_4/Li_4Ti_5O_{12}$ full-cell by coating solid-state electrolyte Li-Al-Ti-P-O. *J. Power Sources* **389**, 240–248 (2018).
36. Fetcenko, M. A. et al. Recent advances in NiMH battery technology. *J. Power Sources* **165**, 544–551 (2007).
37. Evarts, E. C. Lithium batteries: to the limits of lithium. *Nature* **526**, S93 (2015).
38. Xu, K., Zhang, S., Allen, J. L. & Jow, T. R. Nonflammable electrolytes for Li-ion batteries based on a fluorinated phosphate. *J. Electrochem. Soc.* **149**, A1079–A1082 (2002).
39. Suo, L. et al. "Water-in-salt" electrolyte enables high-voltage aqueous lithium-ion chemistries. *Science* **350**, 938–943 (2015).
40. Wang, J. et al. Fire-extinguishing organic electrolytes for safe batteries. *Nat. Energy* **3**, 22–29 (2018).
41. Han, F. et al. Interphase engineering enabled all-ceramic lithium battery. *Joule* **2**, 497–508 (2018).
42. Chen, L. et al. Achieving high energy density through increasing the output voltage: a highly reversible 5.3 V battery. *Chem* **5**, 896–912 (2019).
43. Hayashi, A., Hama, S., Morimoto, H., Tatsumisago, M. & Minami, T. Preparation of Li_2S–P_2S_5 amorphous solid electrolytes by mechanical milling. *J. Am. Ceram. Soc.* **84**, 477–479 (2001).
44. Suo, L., Hu, Y.-S., Li, H., Armand, M. & Chen, L. A new class of solvent-in-salt electrolyte for high-energy rechargeable metallic lithium batteries. *Nat. Commun.* **4**, 1481 (2013).
45. Plimpton, S. Fast parallel algorithms for short-range molecular dynamics. *J. Comput. Phys.* **117**, 1–19 (1995).
46. Frisch, M. J. et al. Gaussian 09, Rev E. 01. Wallingford CT: Gaussian, Inc. (2013).
47. Hohenberg, P. & Kohn, W. Inhomogeneous electron gas. *Phys. Rev.* **136**, B864–B871 (1964).
48. Kresse, G. & Hafner, J. Ab initio molecular-dynamics simulation of the liquid-metal–amorphous-semiconductor transition in germanium. *Phys. Rev. B* **49**, 14251–14269 (1994).
49. Kohn, W. & Sham, L. J. Self-consistent equations including exchange and correlation effects. *Phys. Rev.* **140**, A1133–A1138 (1965).
50. Momma, K. & Izumi, F. VESTA 3 for three-dimensional visualization of crystal, volumetric and morphology data. *J. Appl. Crystallogr.* **44**, 1272–1276 (2011).
51. Humphrey, W., Dalke, A. & Schulten, K. VMD: visual molecular dynamics. *J. Mol. Graph.* **14**, 33–38 (1996).
52. Jakalian, A., Jack, D. B. & Bayly, C. I. Fast, efficient generation of high-quality atomic charges. AM1-BCC model: II. Parameterization and validation. *J. Comput. Chem.* **23**, 1623–1641 (2002).
53. Jakalian, A., Bush, B. L., Jack, D. B. & Bayly, C. I. Fast, efficient generation of high-quality atomic charges. AM1-BCC model: I. Method. *J. Comput. Chem.* **21**, 132–146 (2000).
54. Wang, J., Wang, W., Kollman, P. A. & Case, D. A. Automatic atom type and bond type perception in molecular mechanical calculations. *J. Mol. Graph. Model.* **25**, 247–260 (2006).
55. Chen, F. & Forsyth, M. Elucidation of transport mechanism and enhanced alkali ion transference numbers in mixed alkali metal–organic ionic molten salts. *Phys. Chem. Chem. Phys.* **18**, 19336–19344 (2016).
56. Shimizu, K., Almantariotis, D., Gomes, M. F. C., Pádua, A. A. H. & Canongia Lopes, J. N. Molecular force field for ionic liquids V: hydroxyethylimidazolium, dimethoxy-2- methylimidazolium, and fluoroalkylimidazolium cations and bis(fluorosulfonyl)amide, perfluoroalkanesulfonylamide, and fluoroalkylfluorophosphate anions. *J. Phys. Chem. B* **114**, 3592–3600 (2010).
57. Tsuzuki, S. et al. Molecular dynamics simulations of ionic liquids: cation and anion dependence of self-diffusion coefficients of ions. *J. Phys. Chem. B* **113**, 10641–10649 (2009).

58. Borodin, O. et al. Competitive lithium solvation of linear and cyclic carbonates from quantum chemistry. *Phys. Chem. Chem. Phys.* **18**, 164–175 (2016).
59. Blöchl, P. E. Projector augmented-wave method. *Phys. Rev. B* **50**, 17953–17979 (1994).
60. Perdew, J. P., Burke, K. & Ernzerhof, M. Generalized gradient approximation made simple. *Phys. Rev. Lett.* **77**, 3865–3868 (1996).
61. Kresse, G. & Furthmüller, J. Efficient iterative schemes for ab initio total-energy calculations using a plane-wave basis set. *Phys. Rev. B* **54**, 11169–11186 (1996).

Acknowledgements

This work was supported by the US Department of Energy (DOE) under award number DEEE0008202. The authors acknowledge the University of Maryland supercomputing resources (http://hpcc.umd.edu) made available for conducting the research reported in this paper.

Author contributions

X.F., X.J. and Long Chen designed the experiments and analysed data. X.F., L.C., J.C., T.D., N.P., X.X. and Lixin Chen conducted the electrochemical experiments. X.J. and R.W. conducted the calculations. X.F. and J.C. performed the XPS and Raman analysis. F.H. and J.Y. synthesized the solid-state electrolytes. X.Z. conducted the MPMS analysis. X.F. wrote the draft manuscript. X.F., X.J., Long Chen and C.W. revised the manuscript. C.W. conceived and supervised the project. All the authors contributed to the interpretation of the results.

Competing interest

The authors declare no competing interests.

Additional information

Supplementary information is available for this paper at https://doi.org/10.1038/s41560-019-0474-3.

Correspondence and requests for materials should be addressed to C.W.

Reprints and permissions information is available at www.nature.com/reprints.

Publisher's note Springer Nature remains neutral with regard to jurisdictional claims in published maps and institutional affiliations.